An Observation of the Directional Wave Spectrum Evolution from Shoreline to Fully Developed

EDWARD J. WALSH,* DAVID W. HANCOCK III AND DONALD E. HINES

NASA Goddard Space Flight Center, Wallops Flight Facility, Wallops Island, Virginia

ROBERT N. SWIFT AND JOHN F. SCOTT

EG&G Washington Analytical Services Center, Inc., Pocomoke City, Maryland

(Manuscript received 29 December 1986, in final form 12 December 1988)

ABSTRACT

The Surface Contour Radar (SCR) is a 36-GHz computer-controlled airborne system, which produces ocean directional wave spectra with much higher angular resolution than pitch-and-roll buoys. SCR observations of the evolution of the fetch-limited directional wave spectrum are presented which indicate the existence of a fully-developed sea state. The JONSWAP wave growth model for wave energy and frequency was in best agreement with the SCR measurements. The model of Donelan et al. correctly predicted the propagation direction of waves in the asymmetrical fetch situation nearshore. The Donelan et al. parameterization is generalized to permit other growth algorithms to predict the correct direction of propagation in asymmetrical fetch situations.

1. Introduction

The Surface Contour Radar (SCR) is a 36-GHz computer-controlled airborne radar (Kenney et al. 1979) which generates a false-color coded elevation map of the sea surface below the aircraft in real time. With post-flight data processing it routinely produces ocean directional wave spectra which have much higher angular resolution than pitch-and-roll buoys. The high spatial resolution and rapid mapping capability over extensive areas make the SCR ideal for the study of fetch-limited wave spectra, diffraction and refraction wave patterns in coastal areas, and wave phenomena associated with hurricanes and other highly mobile events. The SCR is also being applied in areas other than producing directional wave spectra such as determining the scattering characteristics of waves and the topography and backscatter characteristics of ice. The SCR is one of the most straightforward remote sensing instruments in measurement concept. It provides great ease of data interpretation since it involves a direct range measurement.

Figure 1 shows the nominal measurement geometry. An oscillating mirror scans a 1.42° half-power width pencil-beam laterally to measure the elevations at 51 evenly spaced points on the surface below the aircraft. The nonscanning receiving antenna is a 1.3° × 40° fan beam with the 40° dimension oriented cross-track. The combination of the transmit and receive antennas narrows the along-track interrogated region to a half-power width of 0.96°. At each of the 51 points across the swath the SCR measures the slant range to the surface and corrects in real-time for the off-nadir angle of the beam to produce the elevation of the point in question with respect to the horizontal reference. The SCR produces these raster scan lines at 20 Hz. Walsh et al. (1985a) described in detail the data processing used to produce directional wave spectra. The SCR spectra are similar to those resulting from stereophotography (Holthuijsen 1983), but the data acquisition and reduction is much easier.

The SCR observations in this paper indicate the existence of a fully-developed sea state and demonstrate the great potential of this remote sensing technique. The ability to obtain contiguous directional wave spectra over a 300 km fetch in less than an hour permits insights to be obtained from a single data set. This is in sharp contrast to the way in which in situ experiments are conducted, where point observations from many different days (or even experiments) are combined in a nondimensional fashion for various wind speeds to arrive at the growth of the wave field with nondimensional fetch.

2. Site and wind history for fetch-limited wave measurements

The mid-Atlantic coast of the United States is shown in Fig. 2 with airport locations indicated for the Wallops

* Presently on assignment at the NOAA/ERL Wave Propagation Laboratory, Boulder, CO 80303.

Corresponding author address: Dr. Edward J. Walsh, 1505 Mapleton Avenue, Boulder, Colorado 80304.

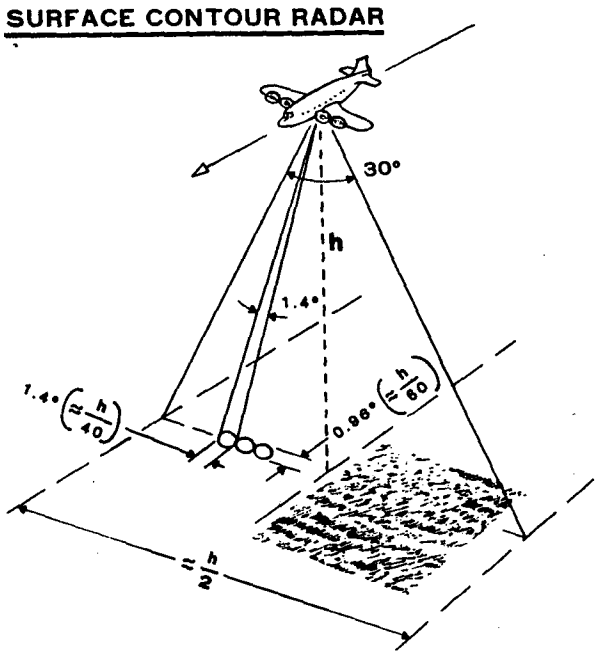

FIG. 1. Nominal measurement geometry of the Surface Contour Radar and the horizontal resolutions in terms of the aircraft altitude, h.

Flight Facility (WFF), JFK, Cape May, and the FAA Technical Center near Atlantic City, New Jersey. Also shown is the location of National Data Buoy Office buoy 44004 (38.5°N, 70.7°W), as well as the location of buoy EB34 in 1976 (40.1°N, 73.0°W). Ground tracks of the NASA P-3 and NOAA P-3 aircraft on 20 January 1983 are shown. A cold air outbreak was occurring when the aircraft took off from WFF. The NASA P-3 flew up the coast to the center of Long Island, then turned and proceeded in the downwind direction for 300 km with the SCR measuring the evolution of the directional wind spectrum with fetch.

The SCR data were acquired during the Marine Air–Sea EXchange (MASEX) experiment, and there has been extensive analysis of the planetary boundary layer (PBL) on that day. The NASA/GSFC Electra aircraft lidar measurements of the PBL (Melfi et al. 1985) indicated that the top of the boundary layer was at approximately a 600 m altitude and virtually independent of fetch for the first 100 km from shore. The NOAA P-3 aircraft made measurements along the perimeter of the box *ABCD* shown in Fig. 2 which indicated the PBL height was approximately 900 m at point *B* and 1100 m at point *C* (Chou et al. 1986). The average value of windspeed measured by the NOAA P-3 at 50 m altitude on legs *AB*, *BC* and *CD* of the box was 11 m s^{-1} (Shu-Hsien Chou, personal communication 1986).

The Long Island shoreline is relatively straight and the contours of constant water depth are approximately parallel to the shoreline in the first 25 km. At greater distances from shore, the depth contours are more nearly parallel to the continental shelf break which runs at approximately 40° in that vicinity.

Figure 3 shows the variation of the water depth versus distance from shore for the NASA aircraft ground track indicated in Fig. 2. Also shown are curves indicating the depth at which waves would begin to "feel the bottom" for various offshore wind speeds. The curves indicate a depth equal to one quarter of the wavelength, λ, associated with the spectral peak frequency, f, (or period, T) using the deep-water dispersion relationship

$$\lambda = g/(2\pi f^2) = g/(2\pi)T^2 \qquad (1)$$

and the empirical fetch dependence for the spectral peak frequency determined in JONSWAP, the Joint North Sea Wave Project (Hasselmann et al. 1973). It is apparent that the water depth would never be a factor in influencing the wave field for offshore winds.

Aircraft observations and surface weather observa-

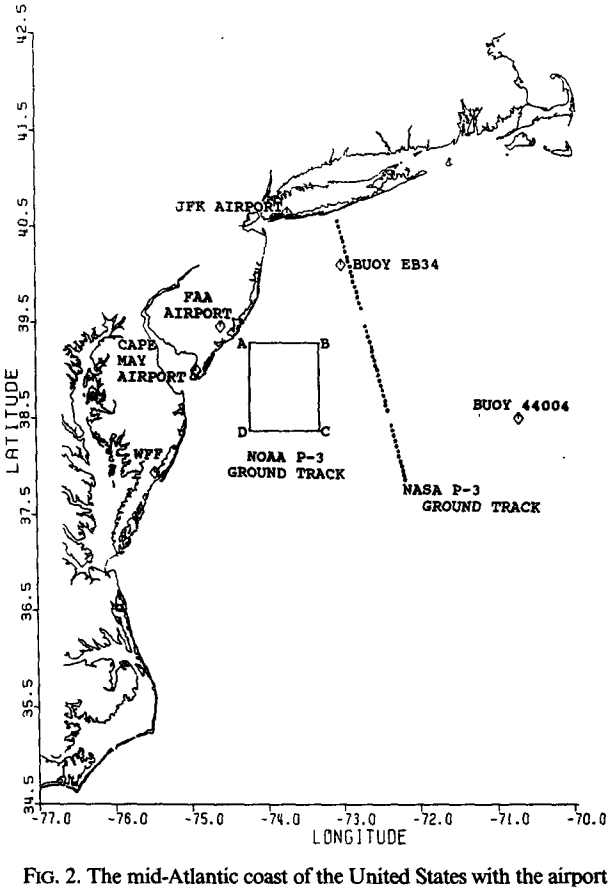

FIG. 2. The mid-Atlantic coast of the United States with the airport locations indicated for JFK, Cape May, the Wallops Flight Facility (WFF), and the FAA Technical Center (formerly NAFEC, the National Aviation Facility Experiment Center). Also shown are the locations of the National Data Buoy Office buoys 44004 and EB34, and the 20 January 1983 ground tracks of the NASA P-3 and NOAA P-3 aircraft.

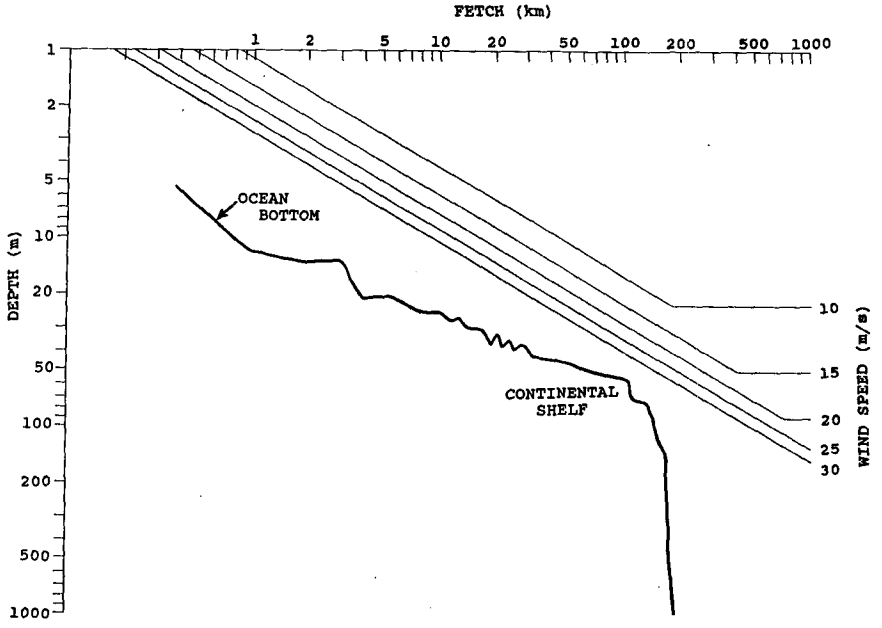

FIG. 3. The variation of water depth versus distance from shore for the NASA aircraft ground track indicated in Fig. 2 and curves indicating the depth at which waves would begin to "feel the bottom" for various offshore wind speeds.

tions obtained from the National Climatic Data Center, Asheville, North Carolina, indicate that the wave growth being studied occurred under unstable atmospheric conditions. Figure 4 shows air temperature observations at the JFK and the FAA airports, and buoy 44004 for the three day period preceding the NASA P-3 flight. The land observations show a significant diurnal variation, especially at the FAA airport, but the air temperature was always significantly colder than the water temperature. The sea surface temperature was 5°C nearshore and increased to 10°C at approximately 150 km from shore along the ground track (from a sea surface temperature Analysis made for the period 15–20 January 1983 by the National Weather Service). Measurements by the NOAA P-3 at 50 m altitude indicate that the mean sea surface temperature along leg *BC* at the time of the flight was 11.5°C and the mean air temperature was −1.2°C.

The air temperature measured at buoy 44004 showed no diurnal variation and varied between about 4° and −2°C. The sea surface temperature measured at buoy 44004 was within 0.3° of 15.9°C during the entire three day period so the water was always 11° to 17°C warmer than the air at that distance from shore.

Figure 5 indicates the wind observations at the JFK and Cape May airports for the three day period pre-

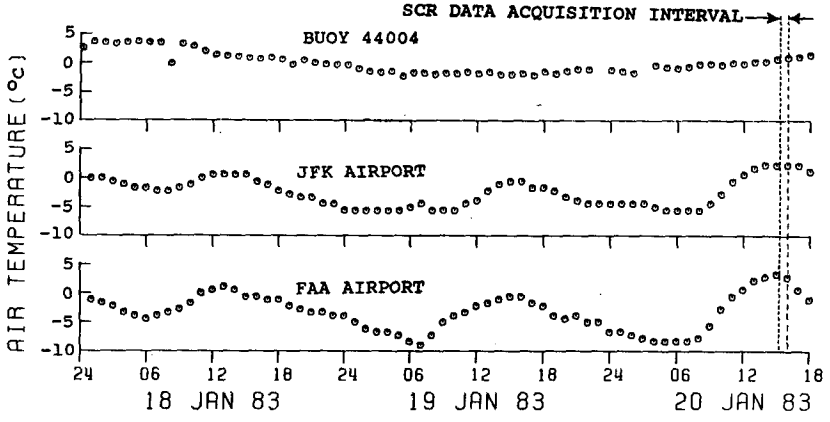

FIG. 4. Air temperature observations for the JFK and FAA airports, and buoy 44004 for the three day period preceding the NASA P-3 flight whose time interval for the downwind leg is indicated by the dotted lines.

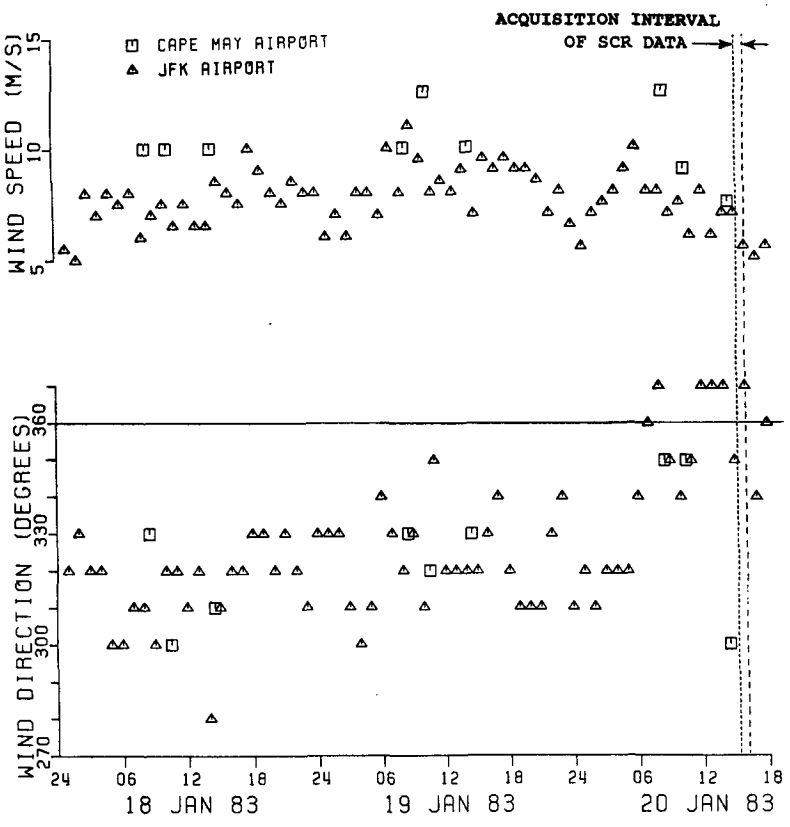

FIG. 5. Wind observations at the JFK and Cape May airports for the three day period preceding the P-3 flight.

ceding the P-3 flight. The observations indicate a spatially homogeneous offshore wind field in direction during the three day period. The wind speeds at JFK read low compared to those at Cape May, but the following discussion indicates that an algorithm for translating the JFK winds into corresponding over-sea values is well known.

The NASA P-3 with the SCR made its downwind run at 440 m altitude which was always well within the PBL. Figure 6 shows the wind speed and direction measured at the NASA P-3 aircraft altitude during the downwind run. The wind direction veered by approximately 10° over the 300 km distance. The wind speed at the aircraft altitude was about 12 m s^{-1} nearshore, increasing to about 13 m s^{-1} at 100 km and then decreasing to a little over 10 m s^{-1} at 300 km. Also shown are the corresponding wind speed observations at JFK Airport and buoy 44004.

Figure 7 shows two sets of curves relating wind observations at the buoy and aircraft altitudes to an equivalent neutral wind speed at 10-m height for various air–sea temperature differences. The curves were calculated using coding obtained from Vincent Cardone. Cardone (personal communication, 1987) feels that the simple surface layer model the coding is based on (Ross et al. 1985) should be applicable up to the NASA P-3 altitude under the atmospheric conditions encountered. The air–sea temperature difference was about −15°C and two points are indicated on the curves corresponding to the 10.2 m s^{-1} aircraft observation and the 9 m s^{-1} buoy observation. The curves indicate that the 10-m equivalent neutral wind speed would be about 1 m s^{-1} higher than the buoy measurement, and about 0.1 m s^{-1} higher than the aircraft measurement. The 10.3 m s^{-1} wind speed extrapolated from the aircraft measurement is in remarkable agreement with the 10 m s^{-1} wind speed extrapolated from the buoy measurement considering that buoy 44004 is some distance from the aircraft ground track (Fig. 2).

At the beginning of the flight line the wind speed at JFK is quite low compared to what would be expected from the aircraft observations. The explanation lies in a study performed by Overland and Gemmill (1977) which included an extensive comparison of the winds measured at JFK and at NOAA buoy EB34. At the time of their study, EB34 was located 60 km offshore and approximately on the downwind leg of the 20 January 1983 flight (Fig. 2). Their comparison covered 792 observations of paired data at 3 h intervals for the five-month period from November 1975 through March 1976 with the 0000 and 1200 UTC data excluded. Wind speeds in excess of 10 m s^{-1}, predomi-

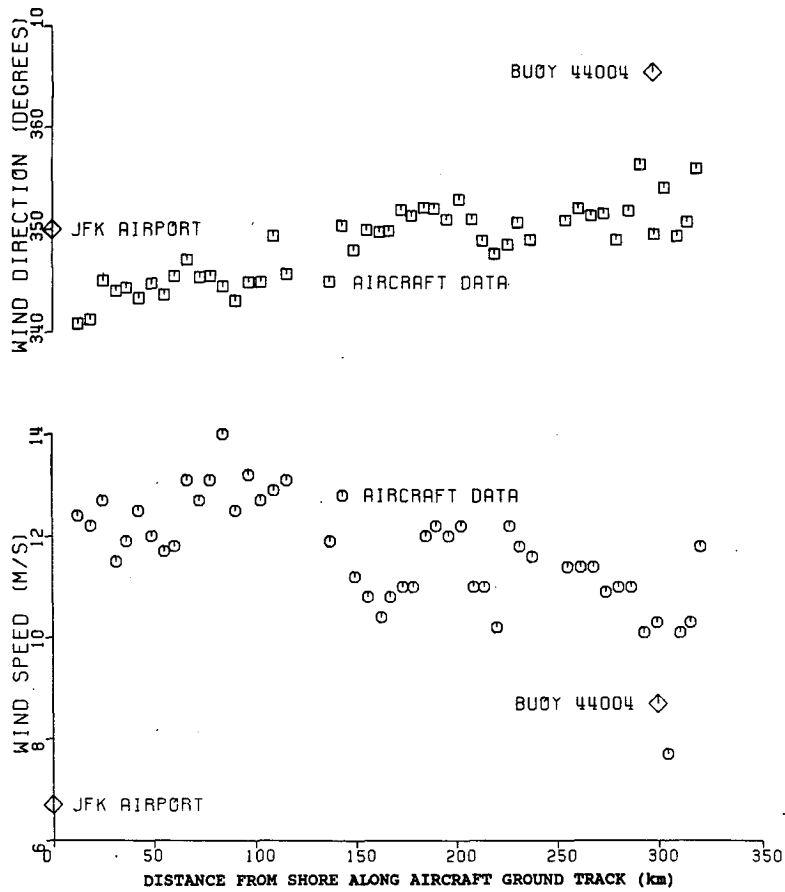

FIG. 6. Wind speed and direction measured at the NASA P-3 aircraft altitude during the downwind run and the corresponding wind speed observations at JFK Airport and buoy 44004.

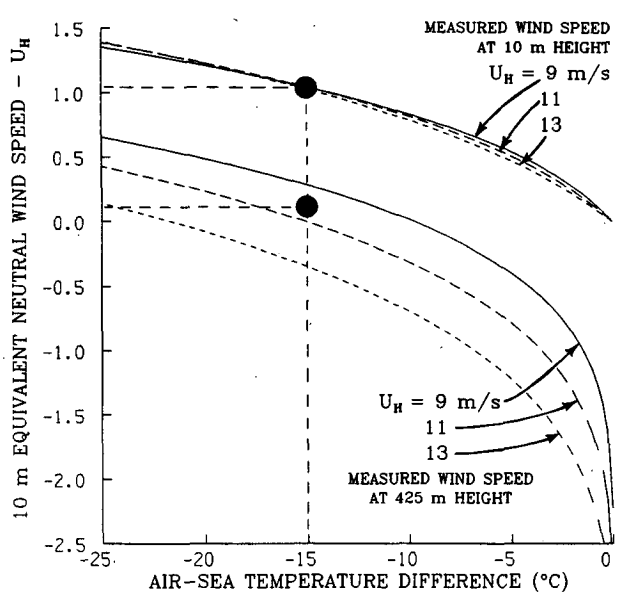

FIG. 7. Two sets of curves relating wind observations at the buoy and aircraft altitudes to an equivalent neutral wind speed at 10-m height for various air–sea temperature differences.

nantly from the north with negative air–sea temperature differences, accounted for 28% of their observations during the five-month period. The equation they derived for the maximum likelihood best fit was

$$U_{EB34} = 0.5 + 1.41U_{JFK} \quad (2)$$

where the wind speeds are in m s^{-1}.

Figure 8 shows a superposition of the wind observations at JFK and buoy 44004 in which the wind speeds at JFK have been converted to over-sea values using (2). With the conversion, the wind speeds and directions at JFK and buoy 44004 are in quite good general agreement over the entire period. The JFK wind directions are only reported in 10° increments and have considerable more scatter than the 8.5 minute buoy averages which are reported to 0.1°.

The FAA airport winds showed the same general variation in direction as JFK but a lower speed. They have not been used because Overland and Gemmill (1977) demonstrated that they are not representative of conditions at sea and concluded that it was because the location of the observations is 36 km inland.

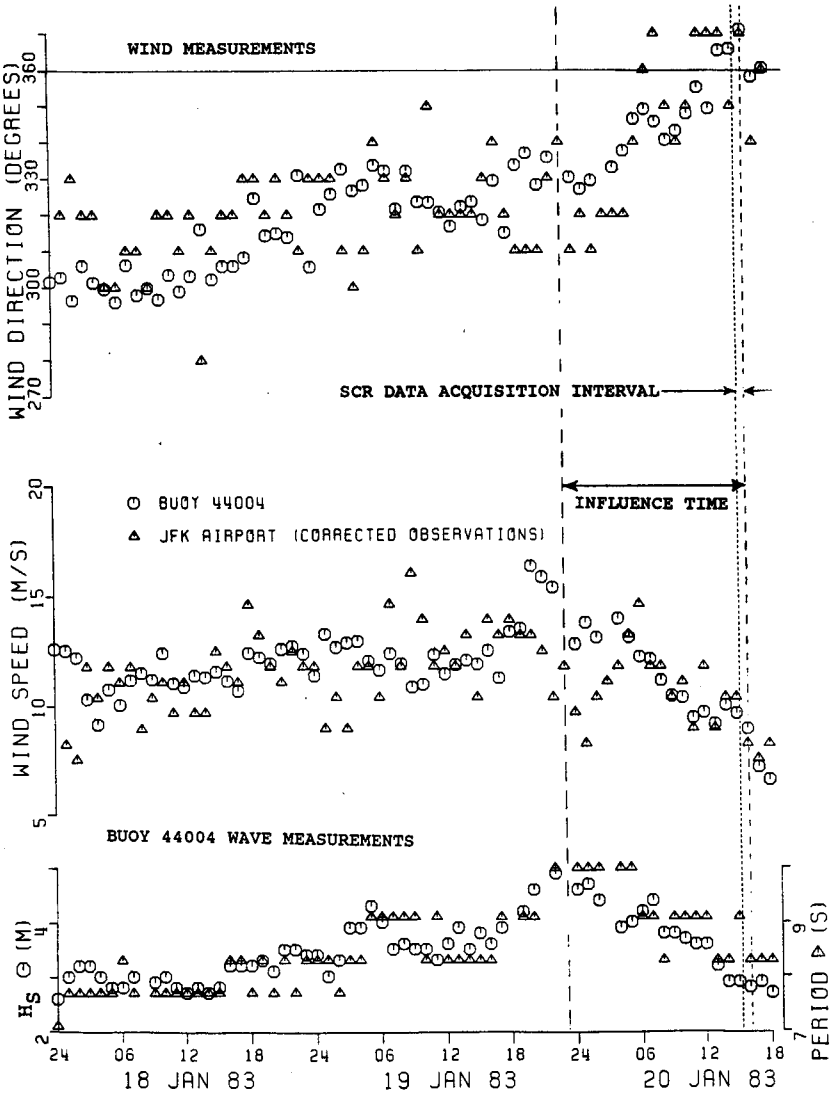

FIG. 8. Superposition of the wind observations at JFK and buoy 44004 in which the wind speeds at JFK have been corrected using (2). Also shown are the wave height and wave period measured by buoy 44004 over the three day period.

The top of Fig. 8 indicates the wind at the beginning of the three-day period started from approximately 300° and, with some minor oscillation, slowly swung around to the north. The vertical dashed lines in Fig. 8 indicate the 45-minute interval during which SCR data were acquired and the 17 hour influence time (calculated in section 4) over which the wind history could affect the observations.

The bottom of Fig. 8 shows the wave height and wave period measured by buoy 44004 over the three-day period. The wave period has a relatively coarse quantization compared to the wave height, but the record shows both of them responding to variations in the wind field. When the wind speed was about 11 m s^{-1} near the beginning of the interval the wave height and period were approximately 2.8 m and 7.8 s. When the wind increased to about 13 m s^{-1} the wave height and period increased to 4 m and 9 s. After the buoy wind speed exceeded 15 m s^{-1} briefly the wave height went up to 5 m and the wave period to 10 s.

The influence time for the SCR observations begins just after the buoy high wind speed observations and over that interval the wind decreased from about 14 to about 9 m s^{-1}. The wave height and period also decreased to approximately the values they had at 1500 on 18 January. It should be noted that although the wind at the buoy did not exceed 15 m s^{-1} for a three hour period, that was 18 hours before the flight and the response of the sea to that event was over at the time the SCR data were taken. We will discuss the variation of wind speed and direction over the influence time in more detail later.

3. Empirical relationships for fetch-limited wave growth

Most of the nondimensional empirical relationships for the evolution of wave frequency and energy for a fetch-limited wave field are of the same form, with the nondimensional quantity to be determined being equal to a constant times the nondimensional fetch raised to a constant exponent. The relationship for nondimensional frequency is

$$\nu = A\tilde{x}_\theta^{-B}. \tag{3}$$

The nondimensional wave frequency and fetch in this paper will be taken to be

$$\nu = fU\rho\cos\theta/g \tag{4}$$

$$\tilde{x}_\theta = X_\theta g/(U\rho\cos\theta)^2 \tag{5}$$

where θ is the angle between the downwind direction and the wave propagation direction, X_θ is the fetch measured in the reciprocal of the wave direction, and ρ is a parameter which will be determined in section 8.

The relationship for nondimensional energy is

$$\epsilon = C\tilde{x}_\theta^{D} \tag{6}$$

where

$$\epsilon = \sigma^2 g^2/(U\rho\cos\theta)^4 \tag{7}$$

and σ is the surface height standard deviation (root-mean-square wave height).

The forms of (4), (5) and (7) are slightly more general than those used by earlier investigators. In the most often used normalization both the $\cos\theta$ and the ρ factors would be set to unity (Hasselmann et al. 1973; Toba 1973; Phillips 1977; Liu and Ross 1980). Donelan et al. (1985, hereafter referred to as DHH) made the important advance of introducing the $\cos\theta$ term in order to be able to deal quantitatively with situations where the fetch was asymmetrically distributed about the wind direction. Figure 9 schematically illustrates their inspiration. If an elongated closed body of water has a steady wind U blowing at some angle to the shore, the rapid increase of fetch as one deviates from the wind direction may more than offset the reduced effectiveness of the wind so that the largest waves approach an observer from some direction other than that of the wind.

The shape of Lake Ontario, where DHH made their observations, is quite elongated and roughly corresponds to an ellipse whose eccentricity is 0.975. Donelan et al. observed waves at the peak of the spectrum propagating as much as 50° off the downwind direction.

When considering the fetch at an angle well off the wind direction, using $U\cos\theta$ assumes that the component of the wind in the direction under consideration is just as effective in generating waves in that direction as if there were only a wind of that magnitude in that direction without the large orthogonal component. Since there are nonlinear interactions, the ρ factor was introduced to allow for the possibility that the effectiveness of a wind component might be different than the DHH assumption. The only limitation placed on ρ at this point is that $\rho = 1$ when $\theta = 0$ so that the growth expressions reduce to those of earlier investigators for the classic fetch-limited case of a wind blowing orthogonal to a straight shoreline.

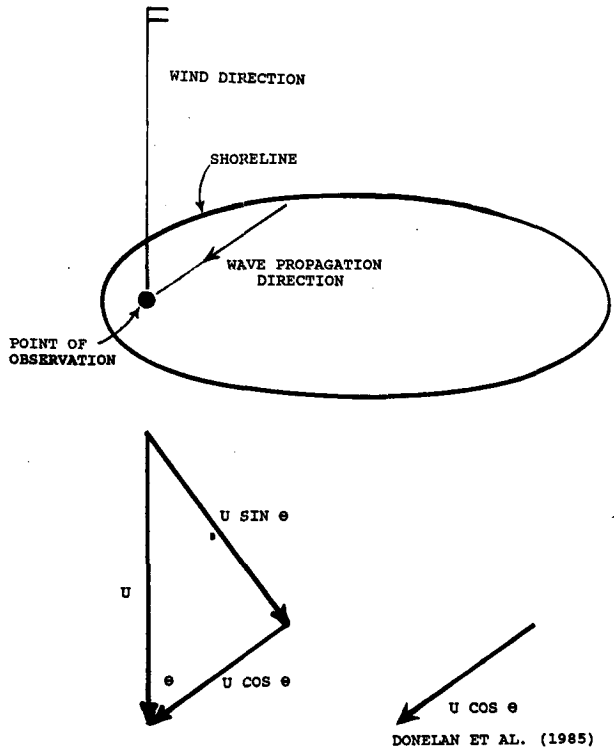

FIG. 9. Fetch asymmetrically distributed about the wind direction on a closed body of water results in the largest waves approaching an observer from some direction other than that of the wind. Donelan et al. (1985) assumed that a wind component could be used in conjunction with the fetch in that direction to determine the wave propagation direction.

It should be pointed out that Huang et al. (1981) suggested a unified empirical relationship for fetch-limited waves by incorporating the steepness of the waves at the peak of the spectrum. In addition to doing an excellent job of reconciling field observations with laboratory measurements, the analysis indicated that A in (3) and C in (6) are not actually constant but vary with wave steepness (and therefore fetch). We will not be incorporating their results in the derivations which follow because it would add to the complexity, and Huang et al. (1981) pointed out that for the range of wave steepness encountered in the field, A and C are very nearly constant.

The constants for (3) through (7) for the four algorithms compared in this paper (Hasselmann et al. 1973;

TABLE 1. Values of constants for various fetch-limited wave growth algorithms.

	A	B	C	D	$D-4B$	$\tilde{x}$	$\tilde{x}/\tilde{x}_{\text{JONSWAP}}$
Hasselmann et al. (1973)			($*10^{-7}$)			for $\nu = 0.133$	for $\nu = 0.133$
(JONSWAP)	3.5	0.33	1.60	1.00	−0.32	20 123	1.00
Present analysis	2.3	0.29	1.86	1.00	−0.16	17 818	0.89
Liu and Ross (1980)	1.9	0.27	1.20	1.10	0.02	18 943	0.94
Phillips (1977)*	1.78	0.25	1.60	1.00	0.00	32 078	1.59
Donelan et al. (1985)	1.85	0.23	8.39	0.76	−0.16	93 538	4.65

* Although Phillips modified the JONSWAP value of B, he let stand the value of D.

Phillips 1977; Liu and Ross 1980; Donelan et al. 1985) as well as the one fitting the measurements presented herein are given in Table 1.

4. Effective windspeed versus fetch

Since the wind varied in both speed and direction, we will compute an effective wind. Because wave generation involves integrals over both space and time, the effective wind will vary with distance from shore. The waves start growing at the shoreline and arrive at the position being considered some time later. That travel time is obtained by integrating the transit time per unit distance (the reciprocal of the group velocity) over the total distance (Bretschneider 1958; Donelan 1980). We will use $(C_g)_P$, the group velocity at the peak of the spectrum, and call the resulting travel time the effective duration, d_e, that the wind has acted on waves which have reached a fetch F. Since the group velocity in deep water is one-half the phase velocity, (1) can be used to arrive at

$$d_e = \int_0^F dX_\theta/(C_g)_P = 4\pi/g \int_0^F dX_\theta/T. \quad (8)$$

If (3), (4) and (5) are used to obtain an expression for the dominant wave period, the result is

$$T = 1/f = U^{1-2B}/(Ag^{1-B})(\rho \cos\theta)^{1-2B} X_\theta^B. \quad (9)$$

Substituting (9) in (8) and integrating results in

$$d_e = 4\pi A F^{1-B}/[(1-B)g^B(\rho \cos\theta U)^{1-2B}]. \quad (10)$$

This relationship between effective duration and fetch is plotted in Fig. 10 for an 11 m s^{-1} wind blowing perpendicular to a straight shoreline ($\rho \cos\theta = 1$) for three of the empirical relationships. The Hasselmann et al. (1973) relationship, hereafter referred to as JONSWAP, becomes fully-developed ($\nu = 0.133$) at 248 km for an 11 m s^{-1} wind and the present analysis reaches that point at 220 km. However, the DHH relationship does not become fully developed until 1155 km, about a factor of five greater.

Once the fully developed state is achieved, the wave height and period no longer grow with increasing fetch. The effective duration continues to increase with fetch, but it takes longer for the effect of the earlier wind to be felt because the waves propagate with the fully developed group velocity instead of a continually increasing group velocity, and the slope of the curves in Fig. 10 increases.

A curve corresponding to a 40 m s^{-1} wind for the empirical relationship fitting the data presented here is also shown to indicate the variation with wind speed. The 40 m s^{-1} wind speed would establish steady state conditions faster at all distances from shore up to the point that the sea state for the 11 m s^{-1} wind became fully developed. This is the same result arrived at by Bretschneider (1958) and Donelan (1980).

When the fully developed duration is attained for the 11 m s^{-1} wind, steady state conditions would have been established at all distances for that wind speed. But the sea state would continue to grow with time for the higher wind speed at distances greater than the fetch-limit of the lower wind speed. Continuing to increase the effective duration for the JONSWAP and present analysis 11 m s^{-1} curves past the fetch at which the wave field becomes fully developed acknowledges

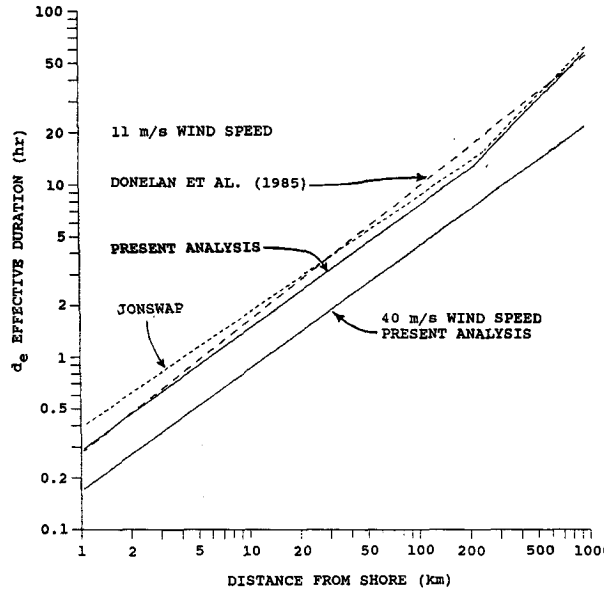

FIG. 10. Relationship between effective duration and distance from shore for an 11 m s^{-1} wind blowing perpendicular to a straight shoreline for three of the empirical relationships, and for a 40 m s^{-1} wind for the algorithm resulting from the present analysis.

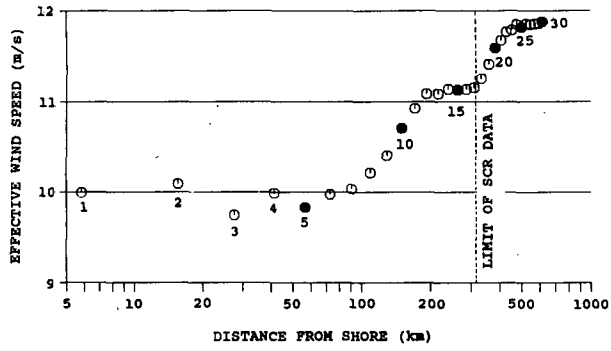

FIG. 11. Effective wind speed versus distance from shore for the time of the SCR flight. The numbers below the data points are the effective duration in hours.

that waves generated from an earlier wind direction could effect the composite wave propagation direction at distances greater than the fetch at which full development is attained.

Figure 11 shows the effective wind speed versus distance from shore for the time of the SCR flight. The effective wind speed was arrived at by taking the average of the wind speed observations from JFK and buoy 44004 and then averaging over various time intervals which always ended at the time of the flight. The averaging time was taken to be the effective duration and the points were placed on the figure at the distance corresponding to the effective duration for the present analysis algorithm shown in Fig. 10 for the 11 m s^{-1} windspeed.

Figure 11 indicates that the effective windspeed was 10 m s^{-1} nearshore, gradually increased to 11 m s^{-1} by 170 km, and then remained constant for the remainder of the SCR data run. This is the motivation for using 11 m s^{-1} in the effective duration algorithm to position the points in Fig. 11, although the result is not sensitive to small changes in wind speed.

Some notes of caution should be sounded at this point. The SCR measurements were made under very unstable atmospheric conditions, while the atmospheric conditions during JONSWAP were stable and the DHH conditions covered a range of stabilities near neutral. The wind field characterization for the SCR data set was also nonideal in other respects, with only two sets of wind measurements over 300 km, and one of them an empirical extrapolation from overland. The wind was not constant over the 17 hour influence time (Fig. 8) but was diminishing and changing direction. Buoy 44004 indicated a change in direction of about 40° and a reduction in speed from about 14 to 9 m s^{-1}.

In making field observations, however, one frequently has to make do with less than the ideal. For example, D. Hasselmann et al. (1980) indicated that well-defined steady meteorological conditions were never encountered during the month of September 1973 when the second JONSWAP experiment took place.

In their analysis of the original JONSWAP experiment, Hasselmann et al. (1973) showed detailed histories of the winds along the measurement profile (their Fig. 2A.1) for five generation cases chosen arbitrarily from the various periods of "ideal" generation conditions. These "ideal" cases typically evidence wind speed variations of 2 to 4 m s^{-1} and direction variations of 30° within distances of 50 km and/or time intervals of six hours. The mean wind speeds for the five cases shown ranged from about 7 to 11 m s^{-1} and the variation was typically about one-third of the mean. In that perspective, the wind variation during the influence time for the SCR data set does not seem quite as bad as it might have at first.

Since Fig. 7 indicates that the 10-m equivalent neutral wind speed would be approximately 1 m s^{-1} higher than the buoy measurements at a −15°C air–sea temperature difference, one could consider using 11 m s^{-1} for an effective 10-m neutral wind speed nearshore and 12 m s^{-1} at full development. On the other hand, since the wind was slowly diminishing, one could make an argument that the wave field could decay continuously, adjusting to the recent wind. In that case 10 m s^{-1} would be an appropriate measured value at full development (see Fig. 8) for which the equivalent neutral windspeed would be 11 m s^{-1}.

The analysis presented in this section and section 2 has been intended to provide a sense of the wind field which generated the waves observed by the SCR and to obtain a nominal value for the wind speed to put the SCR directional wave spectrum observations in perspective. We will use 11 m s^{-1} for that value.

Because of concern about the effective wind speed, it is not intended that this single SCR data set should be used to rewrite much better founded fetch-limited formulae. The SCR data will simply be used to help contrast some of the existing wave growth curves and to motivate a theoretical analysis which can stand by itself. The data will then be used in an example to demonstrate the kind of constraint the theoretical analysis imposes. However, it should be apparent that the SCR has the potential to eliminate the uncertainty in our knowledge of fetch-limited wave growth when participating in an experiment in which the wind field is ideal and well documented.

5. Fetch-limited spectrum evolution

The SCR data were taken on the downwind leg between 2016 and 2103 UTC and consisted of three segments (see Fig. 2). The first segment consisted of 15 minutes of data which was enough to generate 18 nonoverlapping wave spectra. After a three minute gap in which a new magnetic tape was mounted, the second segment was also 15 minutes and generated 18 wave spectra. The second three minute gap to mount the

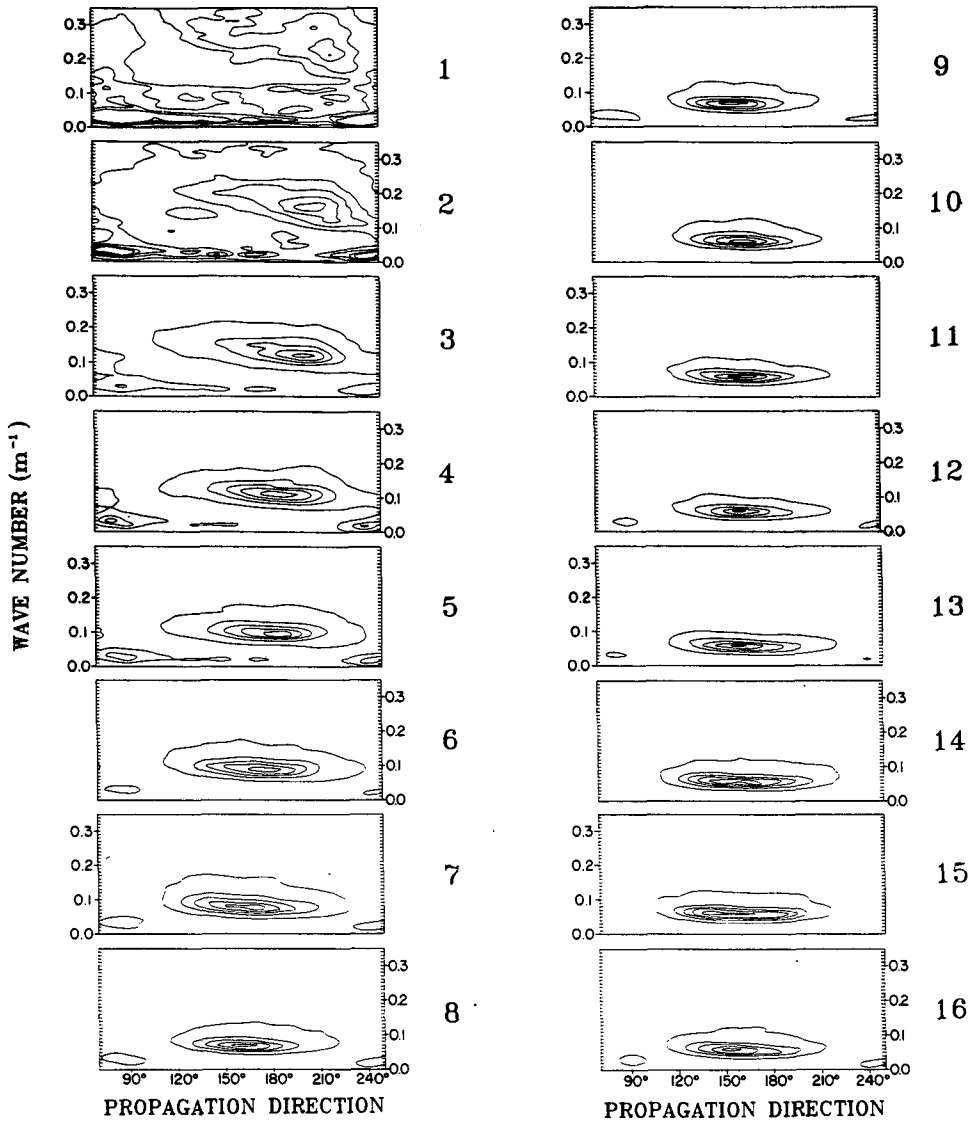

FIG. 12. The entire set of 48 SCR wave spectra from the downwind ground track of Fig. 2 as 16 non-overlapping averages of three spectra. The contours in the spectra are at the 0.1, 0.3, 0.5, 0.7, and 0.9 levels relative to the peak.

third tape was followed by a 10 minute segment, which was used to generate 12 wave spectra. The dots in Fig. 2 indicate the locations of the centers of the nonoverlapping, contiguous data spans used to generate the wave spectra.

Figure 12 shows the entire set of 48 SCR wave spectra from the downwind ground track of Fig. 2 as 16 non-overlapping averages of three spectra. The wavenumber values are 2π over the wavelength. The wave field is referenced to the direction towards which the wave energy is propagating. In this sequence the spectrum evolves quickly at first in shape, wavenumber and propagation direction. But after the 11th or 12th average spectrum there is little change and no trend.

It is seen in Fig. 8 that although JFK Airport reported the wind from 10° for three hours before the start of the downwind leg, the observation just twenty minutes before the leg indicated that the wind was from 350°. That observation was not anomalous because the pilots were told to fly in the downwind direction indicated by the wind streaks at the start of the leg. The direction they chose was 165° whose reciprocal is 345° (remember the JFK directions are quantized to 10°). One can think of the flight proceeding offshore as looking back in time. The local wind generated a downwind wave field which was observed very near the shore. But because of the limited time it had to act, the dominant wave field in the nearshore spectral averages was the one generated during the preceding three hours. As the aircraft progressed farther offshore, the waves backed

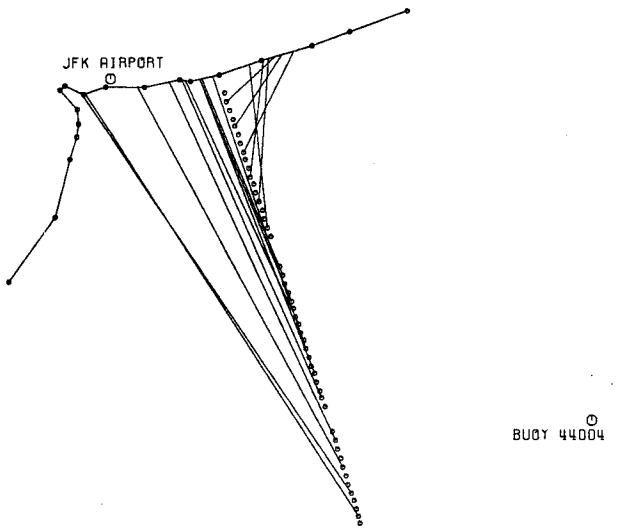

FIG. 13. Radials from the centers of the data spans used to generate the sixteen 3-spectra averages of Fig. 12 are extended in the reciprocal direction of the spectral peak until they intersect the shore of Long Island.

into what had been the prevailing downwind condition at an earlier time.

Figure 13 shows radials from the centers of the data spans used to generate the sixteen 3-spectra averages of Fig. 12, extending in the reciprocal direction of the spectral peak until they intersect the shore of Long Island. It is apparent by the variation of the propagation direction in Fig. 13 that the effect of the wind being from 5° to 10° for the three hour period preceding the start of the downwind leg did not have much of a perturbing effect on the wave spectra at fetches greater than 120 km (the second and third data segments).

Figure 14 shows the growth of H_S (the significant wave height, taken to be four times the surface height standard deviation), versus distance from shore along the aircraft ground track. Measurements are shown from both the SCR and the Airborne Oceanographic Lidar (AOL), another GSFC system on the P-3. The AOL (Hoge et al. 1980) laser system profiled the waves below the aircraft at 250 Hz, compared to 20 Hz for the SCR. The wave height measurements from the two instruments are in excellent agreement except for the two observations nearest shore where the SCR is biased high.

The high pulse repetition frequency of the AOL gives it a distinct advantage over the SCR for determining wave height in situations involving short wavelengths and low wave heights. The AOL data were edited, using a seven-point random-consensus filter to remove outliers, and then averaged. That procedure produced an effective footprint for the AOL of 3.2 m (the ground speed was 114 m s^{-1}) which significantly improved data quality without reducing the amplitude of the waves through spatial filtering. In the comparisons to follow, the measured wave heights will be the average of the SCR and AOL observations in Fig. 14 except for the two observations nearest shore in which only the AOL measurement is used.

Since the AOL did not scan and only profiled the waves, it could not measure the directional wave spectrum. Any noise in the elevation measurements of the SCR would be random and not adversely affect the determination of the peak of the spectrum or its propagation direction even at low wave heights.

6. Comparison of fetch-limited empirical relationships with SCR data

We will first compare the observations of the SCR with the fetch-limited growth rates of several empirical relationships for a wind field blowing orthogonal to a straight shoreline. Under these circumstances both $\cos\theta$ and ρ would be unity. In the following section we will consider the nearshore wave field where the wind was not orthogonal to the shoreline and use that situation to determine ρ.

All of the constants in Table 1 for the nondimensional empirical relationships (3) through (7) were determined by fitting the general relationship to observations and yet each determination of the constants by the various investigators differed from those determined by all other investigators. Some variation is to be expected, but the magnitude of the differences will be seen to be quite surprising.

Pierson and Moskowitz (1964) indicated that a fully developed sea should have a nondimensional peak frequency of 0.14 when the wind speed at 20 m altitude is used in the normalization. In analyzing the JONSWAP data, Hasselmann et al. (1973) indicated 0.14 as a nominal limit even though they dealt only with winds referenced to a 10 m height. Donelan (1980) and DHH appear to correct the nondimensional peak frequency corresponding to the slightly lower winds at the 10-m reference level by using 0.133 instead of the 0.14 value Pierson and Moskowitz (1964) obtained for the 20 m winds. The 0.133 value will be used in the present analysis.

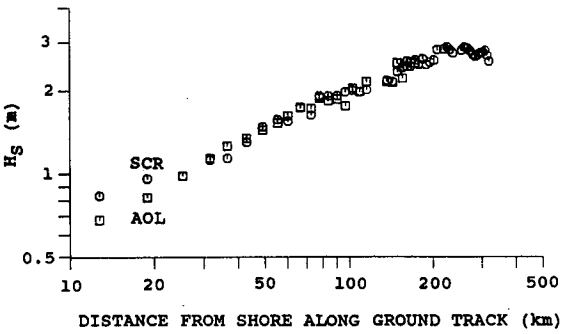

FIG. 14. Growth of H_S versus distance from shore as measured by the SCR and the Airborne Oceanographic Lidar.

Table 1 indicates the nondimensional fetches at which the relationships attain full development and the ratio of those fetches to the JONSWAP fetch. The nondimensional fetch symbols do not have the θ subscript in Table 1 as a reminder that the wind is assumed blowing perpendicular to a straight shoreline. The shortest fetch (0.89 relative to JONSWAP) is for the algorithm resulting from the SCR observations and the longest (4.65) is for the DHH algorithm. This means that for a given wind speed, the predictions for the physical distance at which the sea state becomes fully developed with the same peak frequency differ by more than a factor of five. This variation seems large for algorithms which are all based on observations.

Figure 15 shows plots of the growth of the wave period at the spectral peak and H_S for an 11 m s^{-1} offshore wind for the previously published algorithms indicated in Table 1. Also shown is the variation of the wave period measured by the SCR and H_S measured by the SCR and AOL. The aircraft ground track was approximately orthogonal to the shoreline and the abscissas of Figs. 15 and 16 are labeled distance from shore instead of fetch as a reminder that the wind speed and direction and the wave propagation direction would all affect the nondimensional fetch, and none of them were constant over the data set.

However, Figs. 15 and 16 indicate the relative positions in which the SCR data would most likely have been plotted during the JONSWAP experiment since the fetch was taken to be the perpendicular distance from shore and data for wind directions within 30° of the orthogonal to the shore were included in the scatter plots of fetch versus wave parameters. Furthermore, in another analysis of fetch-limited data, Holthuijsen (1983) labeled a wind field which was 20° off the offshore direction as "ideal."

A relationship for the variation of wave steepness with fetch can be developed that will allow elimination of two of the empirical relationships of Table 1 from further consideration. Equation (7) can be substituted into (6) and the result rearranged to obtain an expression for the rms wave height.

$$\sigma = C^{1/2}(U\rho\cos\theta)^2\tilde{x}_\theta^{D/2}/g. \tag{11}$$

Similarly, (4) and (1) can be used in (3) to obtain an expression for the wavenumber (2π/wavelength) at the spectral peak.

$$k = 4\pi^2 gA^2/(U\rho\cos\theta)^2\tilde{x}_\theta^{-2B}. \tag{12}$$

Equations (11) and (12) can be combined to obtain a measure of the steepness of the wave field:

$$\sigma k = 4\pi^2 A^2 C^{1/2}\tilde{x}_\theta^{(D-4B)/2}. \tag{13}$$

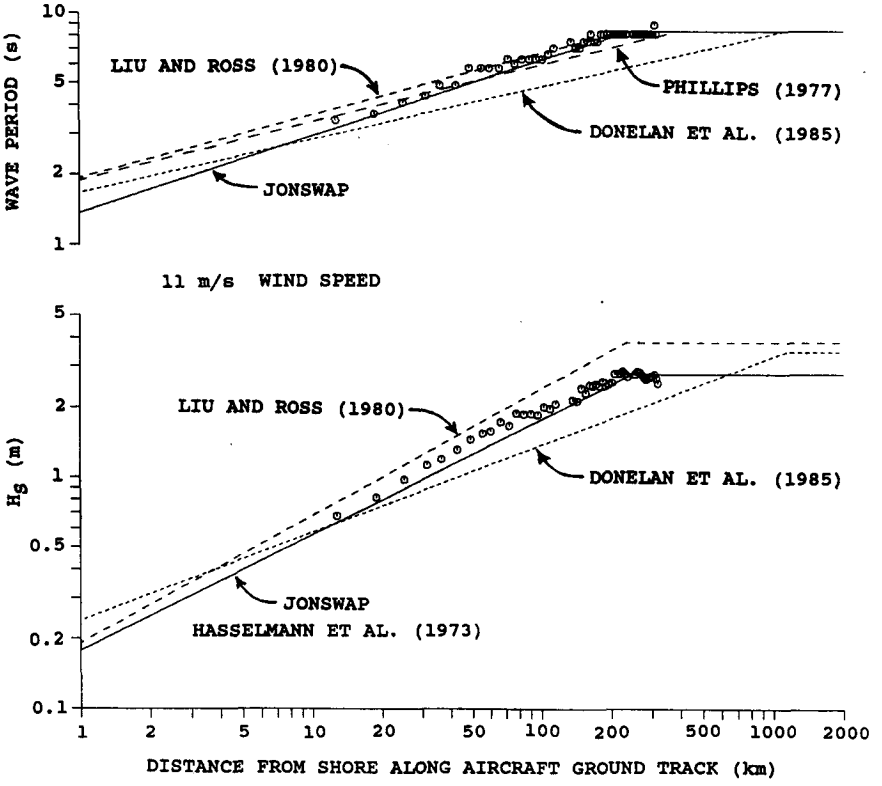

FIG. 15. Fetch-limited growth of wave period and H_S for an 11 m s^{-1} offshore wind for the previously published algorithms indicated in Table 1. Also shown is the variation of the wave period measured by the SCR and H_S measured by the SCR and AOL.

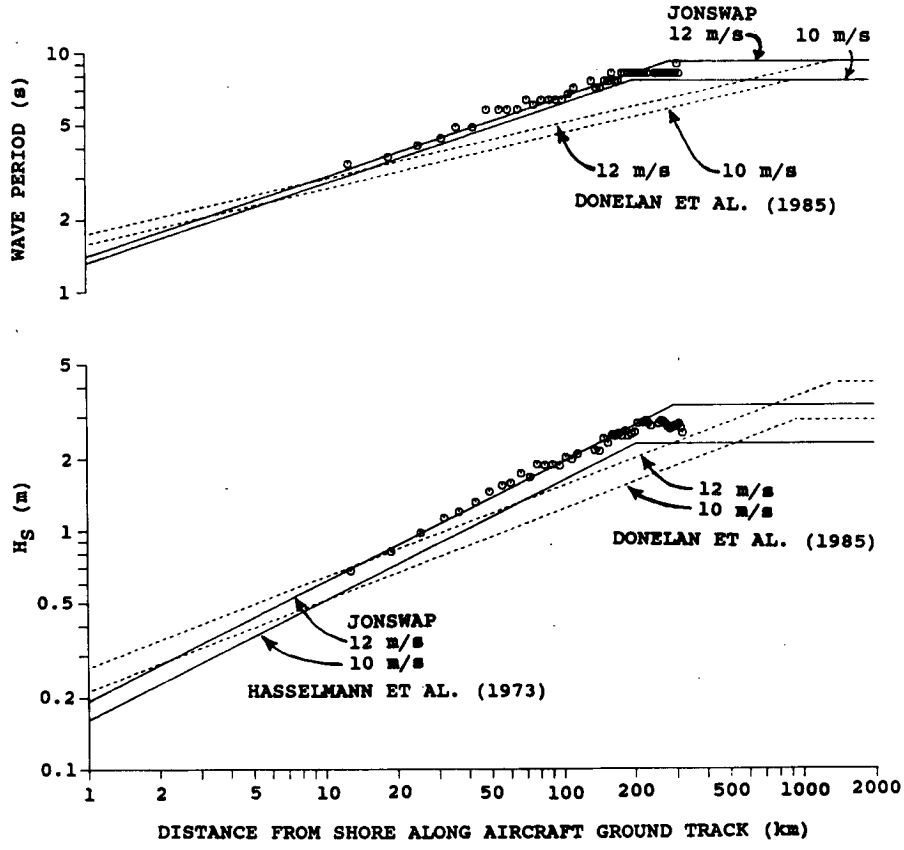

FIG. 16. Measurements of wave period and wave height are compared with the JONSWAP and DHH algorithms for wind speeds of 10 and 12 m s^{-1}. Also shown is the variation of the wave period measured by the SCR and H_S measured by the SCR and AOL.

It is apparent from (13) that the steepness of the wave field will not change if

$$D = 4B. \tag{14}$$

This same result was arrived at by Huang et al. (1981). Since wave steepness is generally observed to decrease with increasing fetch, reasonable empirical relationships should satisfy

$$D - 4B < 0. \tag{15}$$

If the Table 1 values of $D - 4B$ are examined for the relationships, it is seen that Phillips (1977) relationship indicates that wave steepness would not change with fetch (this was first pointed out by Huang et al. 1981) and the Liu and Ross (1980) relationship indicates wave steepness increases with fetch. These two relationships will not be considered further and attention will be focused on the JONSWAP and DHH relationships which indicate wave steepness decreasing with increasing fetch.

In Fig. 16 the SCR measurements of wave period and wave height are repeated for comparison with the JONSWAP and DHH algorithms for wind speeds of 10 and 12 m s^{-1} to indicate the sensitivity of the algorithm predictions to wind speed. At first glance it appears that the JONSWAP algorithm is in quite good agreement with the measurements while the DHH predictions are quite far off with regard to both wave period and wave height. But the situation is not nearly as straight forward as Fig. 16 seems to imply.

Figures 17 and 18, reproduced from Toba (1978), indicate all of the data points used in arriving at the JONSWAP algorithms, as well as additional laboratory data of Toba (1972). Also shown in the figures are the straight lines representing the JONSWAP, DHH, and present analysis algorithms, as well as a curve representing a stochastic form developed by Toba (1978).

The data points exhibit a factor of two or more spread in the nondimensional fetch for observations of the same nondimensional frequency or energy. While this spread may appear small in data which is plotted over six orders of magnitude in nondimensional fetch, it represents a significant amount of error in the individual measurements being used. The DHH measurements show a similar spread. The SCR is not error free (Walsh et al. 1985b), but the errors become far less important when one is using the same instrument essentially instantaneously to measure the wave growth

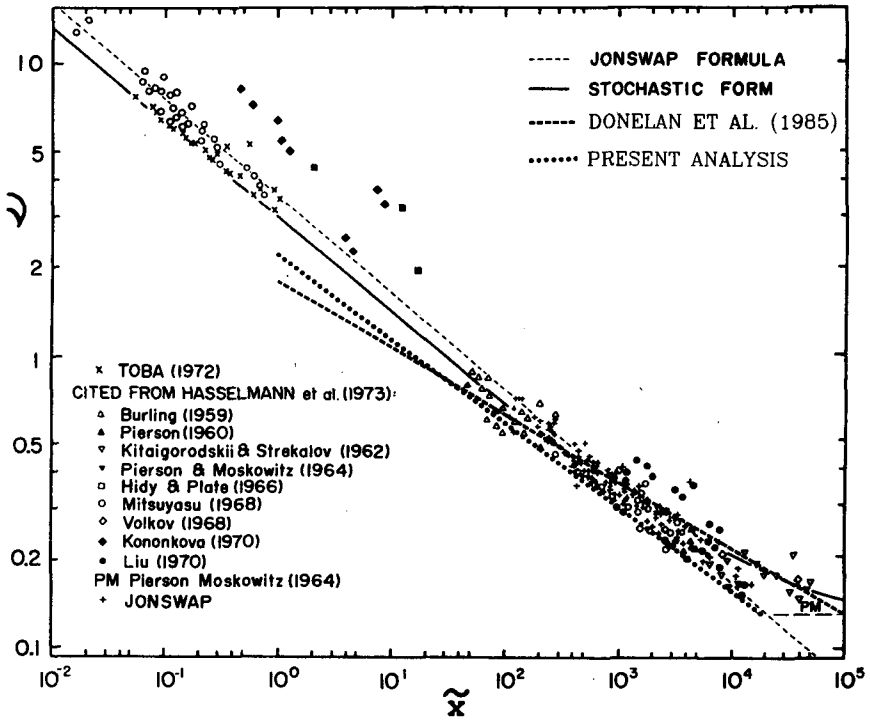

FIG. 17. This figure, reproduced from Toba (1978), indicates the data points used in arriving at the JONSWAP algorithm for nondimensional wave frequency, as well as additional laboratory data of Toba (1972). Also shown in the figure are the straight lines representing the JONSWAP, DHH, and present analysis algorithms, as well as a curve representing a stochastic form developed by Toba (1978).

at all fetches rather than several instruments located at different fetches, or in different countries. Another major advantage the SCR has is in not having to combine uncertainties in the wind field and its history from one day to another.

In examining Fig. 17, it becomes apparent that the slope of the JONSWAP curve was controlled by the laboratory data points of Mitsuyasu because of their position relative to the field data. But Huang et al. (1981) indicated that laboratory and field data should not be combined because of the large difference in wave steepness between the two types of data. If the data for nondimensional fetches less than 30 are excluded in Fig. 17, then the DHH algorithm, whose slope matches the stochastic form of Toba (1978) at a fetch of about 10^3, fits the remaining data points better than the JONSWAP algorithm.

In Fig. 18 it is again apparent that the Mitsuyasu data again had a major impact on the slope of the JONSWAP curve. The DHH algorithm, which again matches the slope of the Toba (1978) stochastic form at a fetch of about 10^3, fits the JONSWAP data points better than the JONSWAP algorithm for nondimensional fetches larger than 10^3. Figures 17 and 18 make the excellent agreement of the SCR observations with the JONSWAP algorithm and the disparity with the DHH algorithm in Fig. 16 seem fortuitous.

7. Asymmetrical fetch situation

We now examine in detail the situation where the variation of the fetch is asymmetrically distributed about the wind direction. It is important to emphasize at the beginning of this analysis that the JONSWAP growth curves presented by Hasselmann et al. (1973) were intended to apply only for orthogonal fetch situations. No attempt was made in JONSWAP to predict the direction of propagation of the waves in asymmetrical fetch situations such as treated by DHH.

Donelan et al. pointed out that if the gradient of the fetch about the wind direction is large, the wave direction will be biased towards the longer fetch. They used (9), with $\rho = 1$, and maximized the right hand side to determine the period, T, at the peak of the spectrum and the wave direction.

For any wind speed U for which the waves are fetch-limited, (9) indicates that the maximum wave period will be achieved by maximizing

$$(\rho \cos\theta)^{(1-2B)} X_\theta^{\,B} \tag{16}$$

or

$$(\rho \cos\theta)^{(1-2B)/B} X_\theta \tag{17}$$

or

$$(\rho \cos\theta) X_\theta^{\,B/(1-2B)} \tag{18}$$

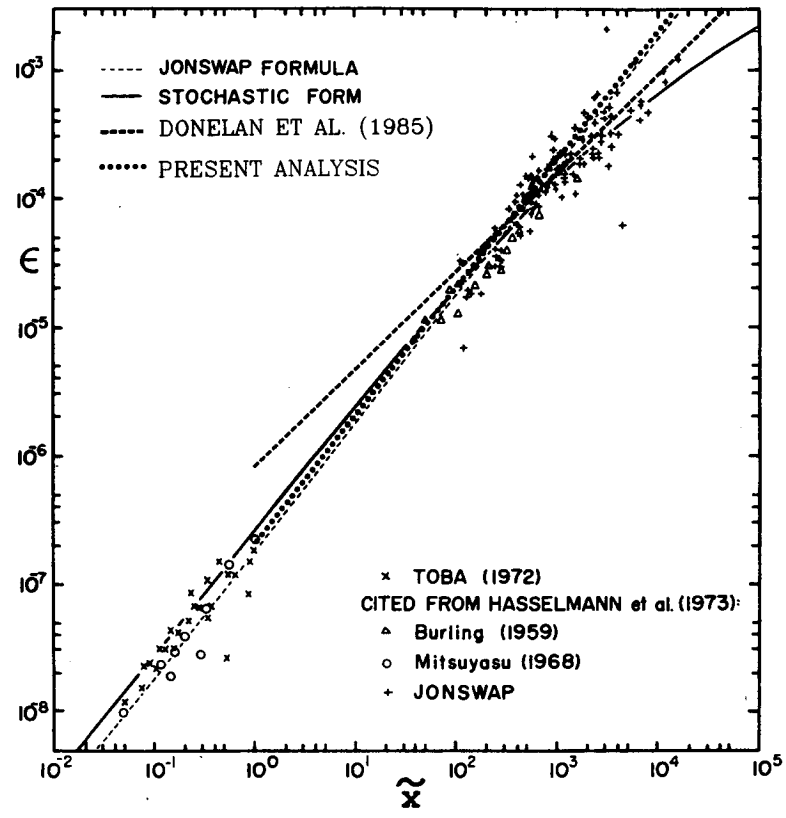

FIG. 18. This figure, reproduced from Toba (1978), indicates the data points used in arriving at the JONSWAP algorithm for nondimensional wave energy as well as additional laboratory data of Toba (1972). Also shown in the figure are the straight lines representing the JONSWAP, DHH, and present analysis algorithms, as well as a curve representing a stochastic form developed by Toba (1978).

since raising (16) to any positive power will not change the angle at which the maximum occurs. Donelan et al. obtained excellent agreement between their observations in Lake Ontario and the predictions of (18), with $B = 0.23$ and $\rho = 1$, for the deviation of the wave propagation direction from the downwind direction.

But the expression for the wave period is not the only thing that could be maximized when there is a gradient of fetch about the wind direction. The wave energy determined from (5), (6) and (7) is

$$\sigma^2 = CU^{(4-2D)}/g^{(2-D)}(\rho \cos\theta)^{(4-2D)}X_\theta{}^D. \quad (19)$$

The wave energy is maximized by maximizing

$$(\rho \cos\theta)^{(4-2D)}X_\theta{}^D \quad (20)$$

or

$$(\rho \cos\theta)^{(4-2D)/D}X_\theta \quad (21)$$

or

$$(\rho \cos\theta)X_\theta{}^{D/(4-2D)}. \quad (22)$$

One might naively expect that the same angle should maximize both wave period and wave energy, but that is not the case. The condition for which both wave period and energy are maximized by the same angle is given by equating (17) and (21),

$$(\rho \cos\theta)^{(1-2B)/B}X_\theta = (\rho \cos\theta)^{(4-2D)/D}X_\theta \quad (23)$$

which requires that B and D satisfy (14), and the wave steepness would not vary with fetch. For realistic situations in which B and D satisfy (15), the angle which maximizes wave period in (18) will exceed the angle which maximizes wave energy in (22).

Wave energy is determined by the integral of the two-dimensional spectrum and the associated direction would be the centroid of the spectrum. This means an asymmetrical fetch situation produces an asymmetrical directional wave spectrum with the peak shifted further off the downwind direction than the centroid of the spectrum. This effect can be observed in the first three spectra in Fig. 12.

Figure 19 indicates the parameters used in the analysis of the asymmetrical fetch situation. The angle between the effective wind direction and the perpendicular to the shoreline is ϕ. The deviation of the wave

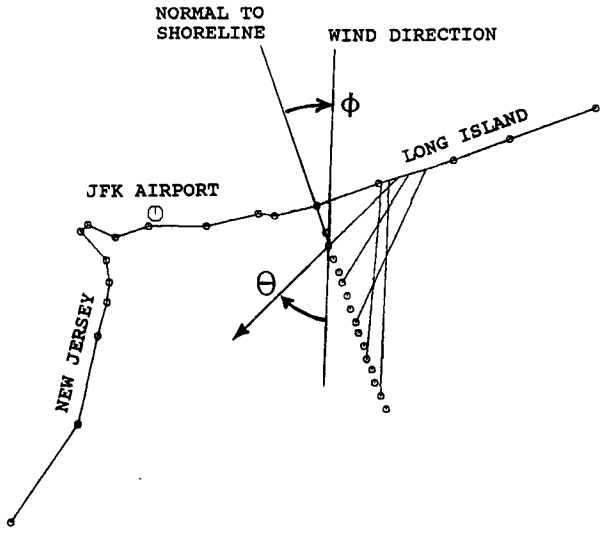

FIG. 19. Parameters used in the analysis of the asymmetrical fetch situation.

propagation direction at the peak of the spectrum from the downwind direction is θ.

Figure 20 shows the variation of the effective wind direction with fetch. The effective wind direction was computed and plotted in the same fashion as the effective wind speed in Fig. 11. Also plotted are the reciprocals of the sixteen propagation directions indicated in Fig. 13 for the three-spectra averages of Fig. 12.

The five wave propagation directions indicated in Fig. 19 (the first five data points in Fig. 20, fetch less than 100 km) provide an excellent opportunity to see if the DHH procedure would predict how much the wave propagation direction at the peak of the spectrum would deviate from the downwind direction for a straight shoreline. Donelan et al. maximized (18) with $\rho = 1$ in predicting the propagation direction to compare with their measurements in Lake Ontario. Because the Long Island shoreline is quite straight, a simulation was performed for a homogeneous wind whose direction deviated by an angle ϕ from the perpendicular to a straight shoreline.

For a straight shoreline, the fetch measured along an angle θ off the downwind direction (which itself is an angle ϕ off the normal to the shore) is proportional to $1/\cos(\theta + \phi)$. Therefore, (18) for a straight shoreline is proportional to

$$\cos\theta/\cos(\theta + \phi)^{B/(1-2B)}. \quad (24)$$

The left side of Fig. 21 shows the variation of (24) with θ for the DHH value of B which makes the exponent in (18) and (24) equal 0.426. There are seven curves shown, corresponding to ϕ values of 1° through 31° in 5° increments. If a curve exhibits a maximum, its location is indicated by a circle. The curves show a maximum for small values of ϕ. As ϕ increases, the location of the maximum shifts away from $\theta = 0$ and the peak broadens. For the larger values of ϕ, the curves increase monotonically.

Although the JONSWAP development did not consider slant fetch situations, we can still inquire what would result from trying to predict the wave propagation direction using the JONSWAP algorithm growth rate and the $U\cos\theta$ parameterization of DHH. The right side of Fig. 21 shows the same family of curves as the left, but for the JONSWAP value of B, which makes the exponent in (18) and (24) equal to 0.971. In this instance, there is no maximum for any wind direction which is even slightly off the normal to the shoreline. This suggests an unstable situation since a wind direction even one degree off the normal to the shoreline would result in the waves nearshore propagating along the shoreline rather than away from it.

Figure 22 shows the loci of the maxima of (24) for the DHH value of B (dashed curve) and nine additional values such that the exponent in (24) took on the values 0.1 through 0.9. For each of the values of B, the wind direction (ϕ) was changed in 0.25° increments from 0° to 50°. For each direction, the angle which maximized (24) was determined using the value of (24) averaged over 30° (±15° about the wind direction as was found to produce optimum results by DHH). Then θ was computed from that angle and the downwind direction. The curves indicate that θ increases monotonically with ϕ up to some value of ϕ for which θ is approximately 20°. The rate of increase of θ with ϕ and the limiting value of ϕ are a function of B. Once the limiting value of ϕ is exceeded, (24) no longer exhibits a maximum and the wave propagation direction is no longer bound to the downwind direction.

The shoreline of Long Island to the east of the SCR starting point runs at approximately 72°. To the west of the starting point it runs at approximately 86° and is more irregular than it is to the east. The orthogonal to the shoreline for waves originating to the east of the starting point would be 342° and for those originating to the west would be 356°. These reference lines are

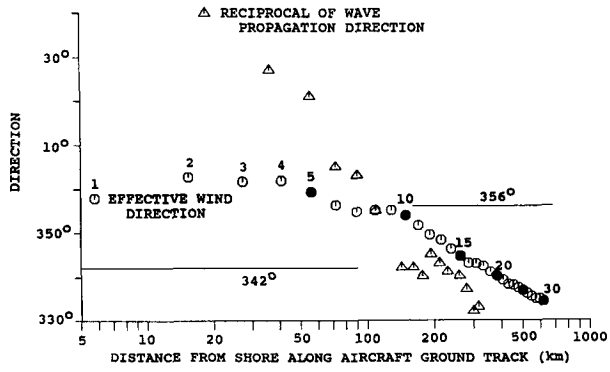

FIG. 20. Effective wind direction versus distance from shore for the time of the SCR flight, and the wave propagation direction measurements made by the SCR. The numbers above the data points are the effective duration in hours.

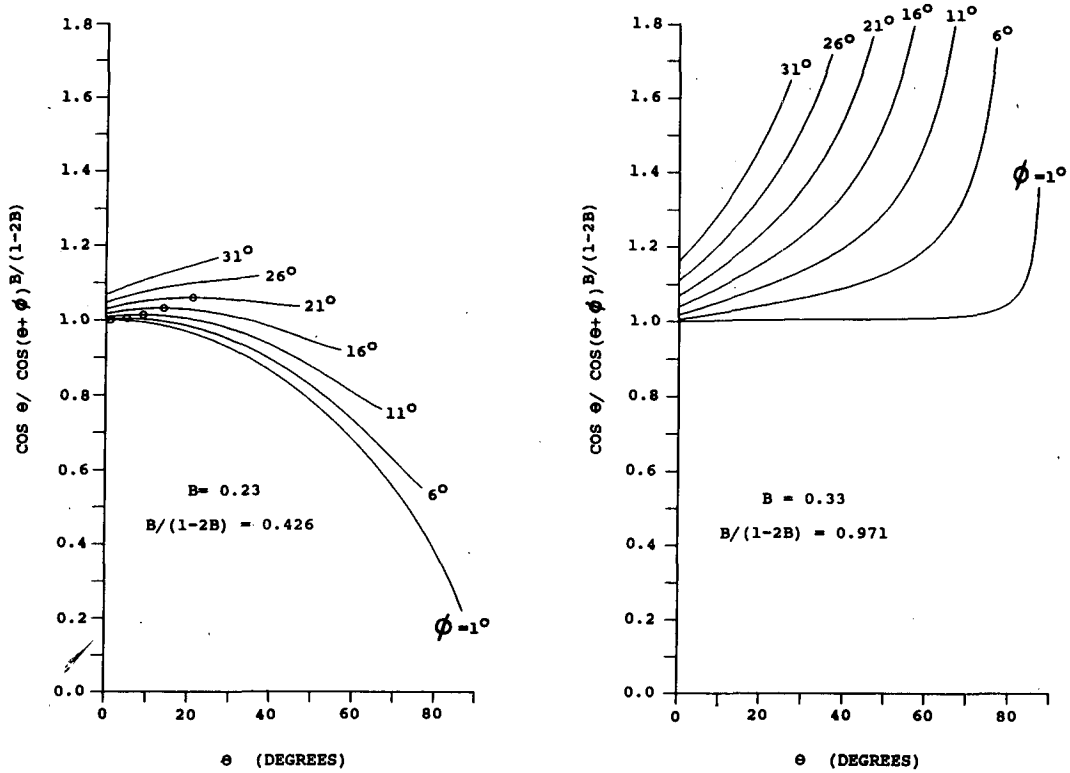

FIG. 21. The variation of (24) with θ for the DHH (left side) and JONSWAP (right side) values of B for various angles ϕ of the wind with respect to the orthogonal to a straight shoreline. If a curve exhibits a maximum, its location is indicated by a circle.

indicated on Fig. 20. To avoid the transition region and any perturbations it might cause in the wave field, we have used only the first five wave propagation data points (fetch less than 100 km) from Fig. 20 to compute ϕ and θ. Those five points have been plotted on Fig. 22. It is remarkable that the DHH algorithm agrees closely with the observations in the bound region since the observed growth rates seem to agree better with the JONSWAP algorithm (Fig. 16).

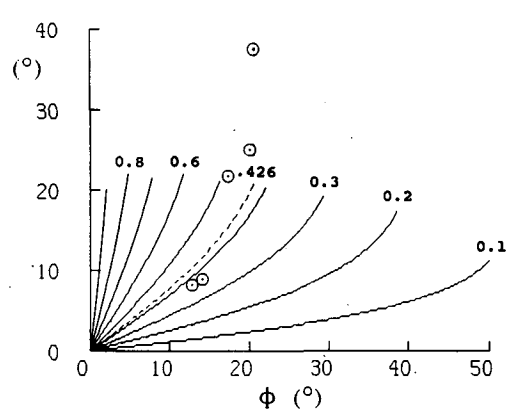

FIG. 22. Predictions of the direction of wave propagation for the DHH algorithm using the DHH growth rate (dashed) and other growth rates, and the SCR observations.

It needs to be emphasized that this asymmetrical fetch analysis and the curves in Fig. 22 are independent of distance from shore only as long as the waves continue to be fetch-limited. Once full development has been achieved, (9) is no longer valid because (3) no longer applies and ν is constant at 0.133. Under those circumstances, (4) can be rearranged to

$$T = 1/f = U\rho \cos\theta/(0.133g). \qquad (25)$$

Since we will show in section 8 that ρ will generally be less than or equal to 1, (25) indicates that the wave propagation direction (maximum T) will occur in the downwind direction ($\rho \cos\theta = 1$).

If the wind began blowing at some angle ϕ to a straight shoreline, the waves at some fixed distance from shore would initially be duration-limited and propagate in the downwind direction. When the wave growth reached its fetch-limit in the downwind direction, the wave field would continue to grow with time in the direction of increasing fetch. The deviation of the angle of wave propagation from the downwind direction would increase with time. If (24) exhibits a maximum, θ would increase until reaching the value indicated by the curves in Fig. 22.

If the value of ϕ exceeds the value for which Fig. 22 indicates a stable solution exists for θ, the value of θ would continue to increase with time until the waves became fully developed. Two effects contribute to the approach to full development at a given distance from shore as the angle off the wind direction increases. First, the actual distance measured along the chosen direction increases as the angle increases. Second, the effective wind speed decreases and (5) indicates that a given distance corresponds to a greater nondimensional fetch.

Waves at points closer to shore would achieve larger values of θ before becoming fully developed than the waves at points farther offshore. Figure 23 indicates the values of θ at which full development is achieved for an 11 m s^{-1} wind as a function of distance from shore. Three curves are shown for different values of ϕ for the algorithm developed later in this paper from the SCR observations. Figure 23 shows that as one approaches a distance from a shoreline at which the wave field would be fully developed for an offshore wind, the waves will propagate in the downwind direction, regardless of its angle to the shoreline.

A ratio of the duration limit at an angle θ off the wind direction to the duration limit in the downwind direction for a wind orthogonal to a straight shoreline can be developed from (10) and is given by

$$d_e(\theta, \phi)/d_e(0, 0) = (\cos(\phi + \theta))^{-(1-B)}(\rho \cos\theta)^{-(1-2B)}. \quad (26)$$

The ratio (26) is independent of fetch but is only valid as long as a fully developed sea state has not been attained. Figure 24 plots the ratio as a function of the angle off the downwind direction for the same algorithm and cases as Fig. 23.

Circles in Figs. 23 and 24 indicate the value of θ for the first SCR data point of Fig. 20. Figure 22 indicates this point was not bound to the downwind direction. Figure 23 suggests that θ could have been about 50°

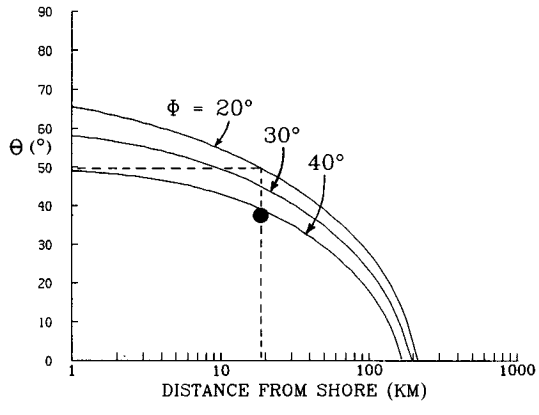

FIG. 23. The values of θ at which full-development is achieved for a 11 m s^{-1} wind as a function of distance from shore. Three curves are shown for different values of ϕ for the algorithm developed later in this paper from the SCR observations.

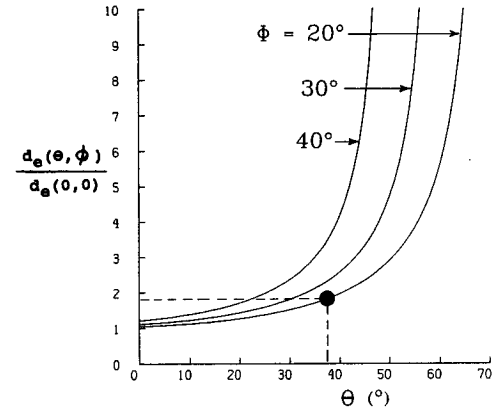

FIG. 24. The ratio of the effective duration versus the effective duration for an offshore wind as a function of the angle off the downwind direction for the same algorithm and cases as Fig. 23.

instead of 37.5° at the 20 km point offshore, but Fig. 24 suggests that θ was not larger because of the short duration of the wind shift. Figure 24 indicates that for θ to reach 37.5° would require 1.8 times the 2.3-h duration indicated in Fig. 20 for waves propagating directly offshore, or about 3.6 hours. Since Fig. 8 indicates that the wind shift at JFK occurred between three and four hours before the flight, that was all the time that was available.

8. Determination of ρ

There can be only one correct solution as to which way the waves will propagate if a constant, homogeneous wind blows at some angle to a straight shoreline. But Fig. 22 (using the DHH analysis technique) indicates that the prediction of wave propagation direction under those conditions is uniquely tied to the growth rate. Because the DHH technique predicted the wave propagation direction both in their Lake Ontario observations and in the SCR data set, we assume at this point that they have the correct answer.

We will now determine ρ such that growth rates other than DHH will be able to make the same prediction for the wave propagation direction as DHH. To make the analysis more convenient we will use (17) instead of (18). We require that valid values of B and ρ in (17) produce an identical expression as (17) for the DHH value of B and $\rho = 1$. Since the physical fetch, X_θ, in (17) is the same in both cases, it drops out and we arrive at

$$(\rho \cos\theta)^{(1-2B)/B} = (\cos\theta)^{(1-2B_d)/B_d} \quad (27)$$

where B_d refers to the DHH value of B from Table 1, and B is the proposed value. Equation (27) requires that

$$\rho = (\cos\theta)^{V_p} \quad (28)$$

where

$$V_p = (B - B_d)/(B_d - 2B_dB). \quad (29)$$

The same procedure could be followed using (21), the expression derived from the wave energy.

$$(\rho \cos\theta)^{(4-2D)/D} = (\cos\theta)^{(4-2D_d)/D_d} \tag{30}$$

Equation (30) requires that

$$\rho = (\cos\theta)^{V_e} \tag{31}$$

where

$$V_e = (D - D_d)/(D_d - D_d D/2) \tag{32}$$

and D_d is the DHH value from Table 1 and D is the proposed value.

For a consistent answer on the azimuthal effectiveness of the wind it follows that

$$V_p = V_e. \tag{33}$$

This does not mean that the angles that maximize wave energy and wave period will be the same. On the contrary, they will differ, the same as they do for DHH. It just means that a single value of ρ must satisfy (3) through (7), not different values for (4) and (7). We can combine (29) and (32) to arrive at the relationship between B and D shown in (34) and plotted as the solid curve in Fig. 25:

$$(B - B_d)/(B_d - 2B_d B) = (D - D_d)/(D_d - D_d D/2). \tag{34}$$

Any combination of B and D that lies on the curve will predict the same propagation direction for the waves in an asymmetrical fetch situation as the DHH algorithm. Also plotted in Fig. 25 is a dashed straight line, which satisfies the expression

$$D - 4B = -0.16. \tag{35}$$

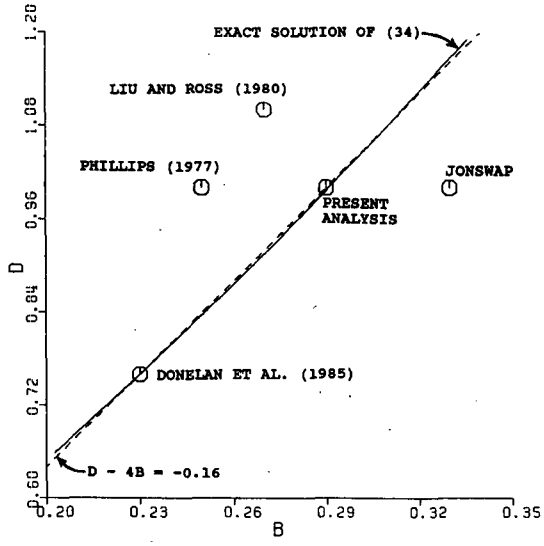

FIG. 25. Relationship between B and D for algorithms predicting the correct propagation direction in asymmetrical fetch situations plotted as the solid curve, and the relationship for various algorithms.

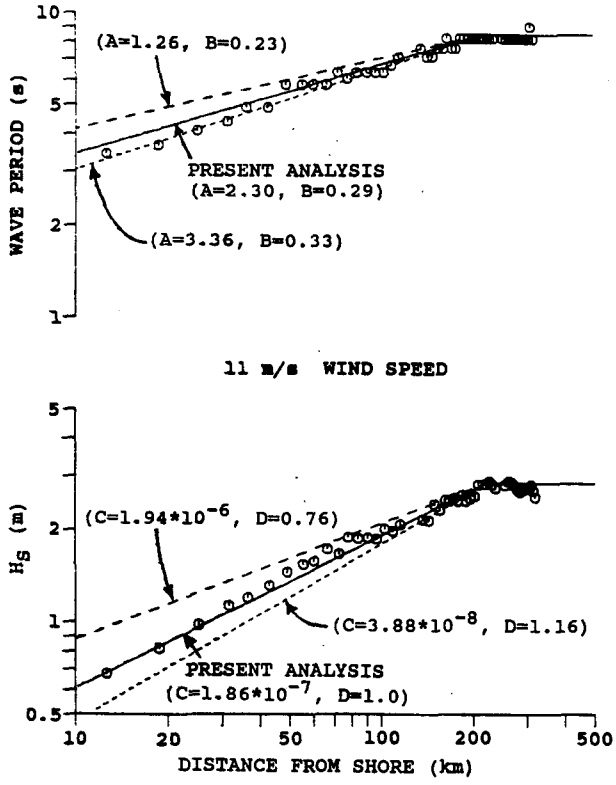

FIG. 26. Proposed algorithm (solid curves) compared with the observations and two other sets of curves for algorithms predicting the correct direction of propagation in an asymmetrical fetch situation.

In the region of interest the two curves are nearly identical. It is interesting that (35) and (13) imply that valid proposed algorithms must have the same percentage change of wave steepness with fetch as the DHH algorithm.

If one examines (29) and (32) in the context of Fig. 25, it is apparent that ρ will be the cosine raised to a positive exponent ($\rho \leq 1$) for all points on the curve in Fig. 25 to the right of the DHH point. The reverse would be true for points to the left of the DHH point, but as the other data points indicate, DHH have reported the lowest values of B and D.

This analysis indicates that one is not free to independently assign the values of B and D when attempting to determine them from a set of observations. Valid combinations of B and D must lie on the curve shown in Fig. 25, which places an additional constraint in determining the best overall match to the data.

Figure 26 uses the SCR data in a demonstration of the effect of this additional constraint. Three sets of curves are shown, with the values of B and D for each set satisfying (35). The values of A and C were adjusted for each of the three sets of curves so they would all agree with the observed fully-developed wave height and period at the same fetch for an 11 m s^{-1} wind speed. The best solution ($B = 0.29$, $D = 1.0$) is indicated

by the solid lines. The other sets of curves correspond to the DHH values ($B = 0.23$ and $D = 0.76$) and the JONSWAP value of $B = 0.33$, which required $D = 1.16$.

Figure 11 indicated that the effective wind speed in the first 100 km was approximately 10 m s^{-1} instead of 11, but correcting for that would not significantly affect the data point positions. For example, the wave period observation closest to shore would have been about 4% higher if the effective wind speed had been 11 m s^{-1}. But this asymmetrical fetch simulation indicated that the observation was about 3% higher than it would have been if the wind were directly offshore. So corrections for the two effects approximately cancel.

The wave height observation closest to shore would have been 10% higher had the wind been 11 m s^{-1} instead of 10. However, the asymmetrical fetch simulation indicated that the observation was about 6% higher than for a wind directly offshore. So the net correction would be to increase the observed wave height value by 4% which is a shift of about half the symbol diameter.

Corresponding to the values of B and D for the model best matching the SCR observations, the value of V is 0.63 and the overall expressions are

$$\nu = 2.3\tilde{x}_\theta^{-0.29} \tag{36}$$

where

$$\nu = fU(\cos\theta)^{1.63}/g \tag{37}$$

$$\tilde{x}_\theta = X_\theta g/(U(\cos\theta)^{1.63})^2 \tag{38}$$

and

$$\epsilon = 1.86\ 10^{-7}\tilde{x}_\theta \tag{39}$$

where

$$\epsilon = \sigma^2 g^2/(U(\cos\theta)^{1.63})^4. \tag{40}$$

Figure 27 compares plots of the $\cos\theta$ azimuthal effectiveness of the wind used by DHH and the $(\cos\theta)^{1.63}$ azimuthal effectiveness for the model presented here. When considering angles significantly off the wind direction, the present model suggests a significantly reduced effectiveness for the wind.

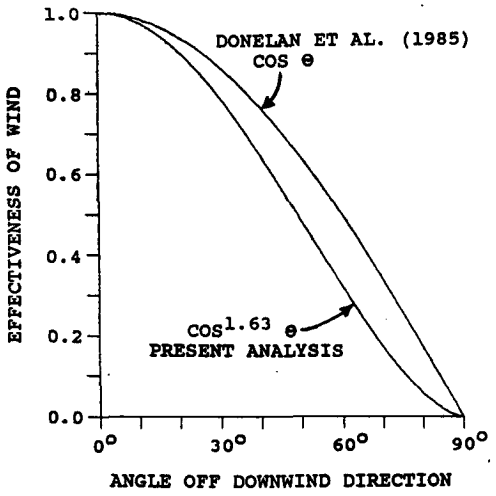

FIG. 27. Comparison of the $\cos\theta$ azimuthal effectiveness of the wind used by Donelan et al. (1985) and the $(\cos\theta)^{1.63}$ azimuthal effectiveness of the present analysis.

9. Conclusions

Surface Contour Radar observations of the fetch-limited directional wave spectrum indicate the existence of a fully-developed sea state. The Donelan et al. (1985) fetch-limited algorithm parameterization has been generalized to allow other wave growth models to predict the same propagation direction in asymmetrical fetch situations. The generalization results in an additional constraint that it is not possible to assign the rate of growth of wave energy independently of the rate of growth of wave period. Matching the model to observations produces an estimate for the effectiveness of a wind component in generating waves which differs from the $U\cos\theta$ model proposed by Donelan et al. (1985) if the wave growth rates differ from their rate.

Acknowledgments. The authors thank Mark A. Donelan, Leonard S. Fedor, Hans Graber, Norden Huang, Frederick C. Jackson, William G. Large, Steven R. Long, James E. Overland, William J. Pierson Jr. and Duncan B. Ross for helpful discussions. A special thanks to Vincent Cardone for his computer program and the attendant discussions. This study was supported by the NASA Oceanic Processes Branch.

REFERENCES

Bretschneider, C. L., 1958: Revisions in wave forecasting: deep and shallow water. *Proc., Sixth Coastal Engineering Conf.*, Council on Wave Research and University of Florida, Gainesville, 30–67.

Chou, S.-H., D. Atlas and E. N. Yeh, 1986: Turbulence in a convective marine atmospheric boundary layer. *J. Atmos. Sci.*, **43**, 547–564.

Donelan, M. A., 1980: Similarity theory applied to the forecasting of wave heights, periods and directions. *Proc. of the 1980 Canadian Coastal Conf.*, Natl. Res. Council Canada, 47–61.

——, J. Hamilton and W. H. Hui, 1985: Directional spectra of wind-generated waves. *Phil. Trans. Roy. Soc. London*, **A315**, 509–562.

Hasselmann, D. E., M. Dunckel and J. A. Ewing, 1980: Directional wave spectra observed during JONSWAP 1973. *J. Phys. Oceanogr.*, **10**, 1264–1280.

Hasselmann, K., T. P. Barnett, E. Bouws, H. Carlson, D. E. Cartwright, K. Enke, J. A. Ewing, H. Gienapp, D. E. Hasselmann, P. Kruseman, A. Meerburg, P. Muller, D. J. Olbers, K. Richter, W. Sell and H. Walden, 1973: Measurements of wind-wave growth and swell decay during the Joint North Sea Wave Project (JONSWAP). *Dtsch. Hydrogr. Z.*, **8**(Suppl. A), No. 12, 7–95.

Hoge, F. E., R. N. Swift and E. B. Frederick, 1980: Water depth measurement using an airborne pulsed neon laser system. *Appl. Opt.*, **19**, 871–883.

Holthuijsen, L. H., 1983: Observations of the directional distribution

of ocean-wave energy in fetch-limited conditions. *J. Phys. Oceanogr.*, **13,** 191–207.

Huang, N. E., S. R. Long and L. F. Bliven, 1981: On the importance of the significant slope in empirical wind-wave studies. *J. Phys. Oceanogr.*, **11,** 569–573.

Kenney, J. E., E. A. Uliana and E. J. Walsh, 1979: The Surface Contour Radar, a unique remote sensing instrument. *IEEE Trans. Microwave Theory and Techniques,* **27**(12), 1080–1092.

Liu, P. C., and D. B. Ross, 1980: Airborne measurements of wave growth for stable and unstable atmospheres in Lake Michigan. *J. Phys. Oceanogr.*, **11,** 1842–1853.

Melfi, S. H., J. D. Spinhirne, S.-H. Chou and S. P. Palm, 1985: Lidar observations of vertically organized convection in the planetary boundary layer over the ocean. *J. Climate Appl. Meteor.*, **24,** 806–821.

Overland, J. E., and W. H. Gemmill, 1977: Prediction of marine winds in the New York Bight. *Mon. Wea. Rev.*, **105,** 1003–1008.

Phillips, O. M., 1977: *The Dynamics of the Upper Ocean,* 2nd ed. Cambridge University Press, 336 pp.

Pierson, W. J., and L. Moskowitz, 1964: A proposed spectral form for fully developed wind seas based on the similarity theory of S. A. Kitaigorodskii. *J. Geophys. Res.*, **69**(24), 5181–5190.

Ross, D. B., V. C. Cardone, J. Overland, R. D. McPherson, W. J. Pierson, Jr. and T.-W. Yu, 1985: Ocean surface winds. *Advances in Geophysics,* Vol. 27, Academic Press, 101–140.

Toba, Y., 1972: Local balance in the air–sea boundary process. I: On the growth process of wind waves. *J. Oceanogr. Soc. Japan,* **28,** 109–120.

——, 1973: Local balance in the air–sea boundary process III: On the spectrum of wind waves. *J. Oceanogr. Soc. Japan,* **29,** 209–220.

——, 1978: Stochastic form of the growth of wind waves in a single-parameter representation with physical implications. *J. Phys. Oceanogr.*, **8,** 494–507.

Walsh, E. J., D. W. Hancock, D. E. Hines, R. N. Swift and J. F. Scott, 1985a: Directional wave spectra measured with the Surface Contour Radar. *J. Phys. Oceanogr.*, **15,** 566–592.

——, ——, ——, —— and ——, 1985b: Elimination of directional wave spectrum contamination from noise in elevation measurements. *IEEE J. Oceanic Eng.*, **OE-10,** No. 4, 376–381.